Plasticity and brittleness of the ordered beta-0 phase in a TNM-TiAl alloy

Guy Molénat, Benjamin Galy, Michael Musi, Jean-Philippe P Monchoux, Louise Toualbi, Helmut Clemens, Marc Thomas, Alain Couret

Plasticity and brittleness of the ordered β_o phase in a TNM-TiAl alloy

Guy Molénat [a,*], Benjamin Galy [a], Michael Musi [b], Louïse Toualbi [c], Marc Thomas [c], Helmut Clemens [b], Jean-Philippe Monchoux [a], Alain Couret [a]

[a] CEMES, Université de Toulouse, CNRS, 29 rue Jeanne Marvig, BP 94347, 31055 Toulouse, France,

[b] Department of Materials Science, Montanuniversität Leoben, Franz-Josef-Straße 18, 8700 Leoben, Austria

[c] ONERA/DMAS Université Paris Saclay, 29 Avenue de la Division Leclerc, BP 72, 92322 Châtillon Cedex, France

* Corresponding author

Abstract

In order to identify the reasons for the brittleness of a TNM-TiAl alloy ($Ti_{51.05}Al_{43.9}Nb_4Mo_{0.95}B_{0.1}$ in at.%), the plastic deformation behaviour of the ordered β_o phase is investigated. The corresponding powder was densified by Spark Plasma Sintering to produce a near lamellar microstructure made of γ/α_2 lamellar colonies surrounded by γ and β_o grains. Then, the room temperature tensile behaviour is studied by carrying out tensile tests and additional in-situ straining experiments in a transmission electron microscope (TEM). The TNM alloy exhibits a limited ductility, with the fracture surface of test specimens showing cleavage facets along lamellar interfaces. In addition, the β_o grains contain nano-precipitates of the ω_o phase and deform plastically by <111> superdislocations dissociated into two superpartial dislocations separated by an antiphase boundary. These dislocations glide in {011} planes and are observed to be localized into pile-ups, which is related to the ω_o strengthening

precipitation within the β_o grains. This localised hardening behaviour leads to stress concentration in grain boundaries which is assumed to be responsible for delamination along lamellar interfaces in neighbouring lamellar colonies.

Keywords: A. titanium aluminide alloys; B. brittleness and ductility, dislocation structure, plastic deformation mechanisms; C. powder metallurgy; F. transmission electron microscopy;

1. Introduction

The new generation of intermetallic γ-TiAl-based alloys suitable for high-temperature structural applications usually contains refractory elements in order to improve mechanical properties at elevated temperatures via the reduction of dislocation mobility. These elements, e.g. V, Nb, Cr, Mo, Re or W, also promote the formation of the body-centred cubic (bcc) phase as disordered β phase (A2 structure) at high temperatures and ordered β_o phase (B2 structure) at lower temperatures. As mentioned in the exhaustive review of Appel et al. [1] on TiAl alloys, the role of this phase on mechanical properties is still unclear: "*A possible concern for the β-solidifying alloys is the reported reduction in mechanical properties such as room temperature ductility, high-temperature strength and creep resistance associated with the presence of the β/B2 phase*s". A review of the current literature does confirm that the ductility of these β/β_o phases remains an open question.

Indeed, on one hand, the β_o phase is considered to present very limited plastic deformation. In a Nb and Mo containing TiAl alloy, Hoppe et al. [2] showed a dislocation-free β_o grain located between two deformed lamellar colonies and assumed that an elastically transmitted deformation occurs between colonies promoted by a high internal stress. In-situ high-energy X-ray diffraction tensile experiments were performed at room temperature (RT)

on sheets of the so-called TNM-TiAl alloy with a nominal composition of Ti-43.5Al-4Nb-1Mo-0.5B (in at.%) [3]. In this study, a linear variation of the lattice strain for the β_o-reflections was found as a function of the applied stress, which was interpreted as indicativeof no plastic deformation in this phase. Sun et al. [4] measured the tensile behaviour of TiAl alloys with different amounts of Fe, Cr, V and Nb and found a decrease in plastic elongation with the increase in the content of alloying elements, which is associated with an increase in the proportion of β_o phase. Based on the observation of cleavage fracture facets in β_o grains and despite the presence of dislocations, these authors concluded to the brittleness of this phase.

On the other hand, Morris et al. [5, 6] investigated the RT mechanical properties of a Ti-44Al-2Mo (at%) alloy which shows that plastic elongation (0.5%) was higher in the as-HIPed condition with a higher β_o phase volume fraction (15%), compared to the other process conditions. Besides, these authors observed two types of dislocations in the β_o grains: <100> dislocations and dissociated <111> superlattice dislocations, which formed pile-ups nucleated at grain boundaries under the effect of deformation in adjacent grains. Th limited ductility of this alloy was attributed to both a low mobility of dislocations in the β_o phase and the lack of slip activity in the α_2 phase. Finally, Leitner et al. [7], who listed all the microstructural features playing a role on the fracture toughness of β_o containing TNM-TiAl alloys, did propose a negative effect of this phase as it forms a continuous seam at lamellar colony boundaries.

Based on these discrepancies in the literature about the role of the β_o phase on plasticity and fracture properties of γ-TiAl based alloys, the present work aims at clarifying this open question by combining an experimental approach of post-mortem and in-situ Transmission Electron Microscope (TEM) observations.

For this purpose, a pre-alloyed powder with the chemical composition of the TNM-TiAl alloy, $Ti_{51.05}Al_{43.9}Nb_4Mo_{0.95}B_{0.1}$, in at.%, was densified by Spark Plasma Sintering (SPS). The

metallurgical features and mechanical properties of this alloy family are summarised elsewhere [8, 9]. Consistently with the Nb and Mo contents, the β/β_o phase is a constituent of this alloy associated with the γ and α_2 phases.

In TiAl alloys, the β-stabilizing element Nb limits the formation of the γ-TiAl phase ($L1_0$ structure) and shifts the β and β_o phase field region to higher Al concentrations. The β_o phase is known to transform into ω-type phases at temperatures ranging between 500 °C and 1100 °C, depending on alloy composition and thermal treatments [10, 11]. This transformation of ω-type hexagonal phases in bcc phases is similar to that commonly observed in commercial β or near-β Ti base alloys [12-17], or more generally in alloys of group IV elements such as Ti, Zr and Hf [17-19]. The transformation occurs through local chemical rearrangements associated with the collapse of {111} bcc planes, leading to the formation of double layers, the latter alternating with single layers. Because there are four $\{111\}_{\beta o}$ planes in a single grain, four rotational orientation variants can be generated.

In the case of intermetallic TiAl alloys, extensive research has been done to determine the completeness of the bcc/hexagonal transformation, as well as the related chemical rearrangements [20-23]. In particular, this transformation was investigated in a cast TNM alloy with a chemical composition similar to that of the alloy studied here [21,23]. In-situ high-energy X-ray diffraction heating experiments allowed Schloffer et al. [21] to measure the solvus temperature of ω_o phases to be 825 °C. Klein et al. [23] proposed that the growth sequence was dominated by the redistribution of Mo into the β_o matrix, i.e. by the Mo diffusivity.

2. Materials and methods

The pre-alloyed TNM powder produced by argon gas atomization with the Electrode Induction Melting Gas Atomization (EIGA) technique [24] was densified by SPS using the thermal and pressure cycle described elsewhere [25]. To achieve a lamellar microstructure containing β_o grains, the dwell temperature ranged between 1300 °C and 1360 °C [26]. Throughout the paper, the indicated temperatures correspond to the actual temperatures of the powder and material (for detailed information regarding the SPS process the reader is referred to Ref. [25]). Cylindrical billets with a 36 mm diameter and an 8 mm thickness were sintered under four different conditions: three different dwell temperatures, one of them (1360 °C) repeated with a 60 min instead of the usual 2 min (see Table 1). No heat treatment was applied to the material after sintering. Three specimens suitable for RT tensile tests (10^{-4} s^{-1} strain rate) were machined from each billet.

A JEOL 6490 Scanning Electron Microscope (SEM) was used to characterize the microstructures in back-scattered electron (BSE) mode, and to analyse the fracture surfaces in secondary electron (SE) mode. Electron dispersive spectroscopy (EDS) analyses were performed with a FEI Helios 600i SEM equipped with an Oxford detector. The volume fractions of the β_o phase in the different materials were measured by X-ray diffraction (XRD) analysis on an AXS D8 Advanced diffractometer from Bruker. A JEOL 2020 TEM operating at 200 kV was used to analyse both the dislocations microstructures generated by the tensile tests (post-mortem microscopy) and the controlling dislocations mechanisms (in-situ RT straining experiments) with a Gatan straining holder). Every TEM samples for both post-mortem and in-situ experiments were taken from the AM504 billet (Table 1).

3. Microstructure of the as-SPSed TNM alloy

Regarding the four billets under examination (Table 1), it appears that billet AK639 with the lowest dwell temperature exhibits a lower volume fraction of the β_o phase compared to the three other billets. Billet AM504 with a specific long duration at dwell temperature shows larger lamellar colonies. The common microstructural feature for the four materials corresponds to large lamellar colonies with β_o grains along boundaries (see Fig. 1). As described in section 4, these similar microstructures result in similar RT mechanical behaviour (Fig. 3).

Regarding the lamellar microstructure, electron backscatter diffraction (EBSD) fails to delimit the colony size since this technique analyses each lamellae of a given colony as a different grain (indeed, in a colony the lamellae can take six different orientations, which manifest in ordered domains, twins or pseudo-twin relationships [27]). Therefore, the colony size has been measured using a manual procedure applied on SEM micrographs. For each measurement, one hundred adjacent colonies were isolated and their size measured using the free ImageJ software. The grain size is defined as the diameter of a circle with the same area as the respective colony. The average values as well as the corresponding standard deviations (σ) are summarized in Table 1 for the four specimens. The relatively high value of σ (in the order of half the average colony size) reflects a large scattering of the colony sizes that typically range from a few microns to nearly one hundred µm., The volume fraction of the β_o phase as measured by XRD is also reported in Table 1, does increase with dwell temperature up to 1325 °C and then remains more or less constant.

Table 1

Microstructural characterization of the obtained as a function of the SPS dwell temperature.

Dwell temperature (°C)	1300	1325	1360	1360 - 60 min -
Specimen designation	AK639	AN849	AL824	AM504
Other SPS billets used in the study		AK746 AM797		
Average colony size (µm)	17.27	17.38	17.11	28.04
Standard deviation (µm)	11.27	9.07	8.95	13.15
Vol.% of the β_o phase	5.6	8.2	8.4	9

Therefore, the microstructure presented in Fig. 1 (billet AK746 for SEM analysis, Figs. 1a-e, and billet AM 504 for TEM image of Fig. 1f) is representative for the different sintered materials. The SEM micrograph of Fig. 1a shows a near lamellar microstructure made of γ/α_2 lamellar colonies surrounded by borders with γ and β_o grains exhibiting black and white colours, respectively. The β_o phase is distributed in different ways as evidenced by the corresponding enlargements (Figs. 1b-e) of Fig. 1a:

- Extended shapes, situated at junctions between colony boundaries (enlargement framed in yellow, Fig. 1b),
- Elongated features, generally located along a boundary between a border and a lamellar colony (enlargement framed in red, Fig. 1c),
- Series of parallel, elongated and thin noodle-shaped phase immerged in a γ grain, generally oriented perpendicularly to the boundaries (enlargement framed in blue, Fig. 1d),
- Small precipitates, lath- or noodle-shaped (enlargement framed in orange, Fig. 1e) and,
- Bright zones located inside lamellar colonies (bright arrows in Fig. 1a).

Figure 1f shows a TEM micrograph of an area with the β_o phase distributed at the junction between several colony boundaries according to the situation illustrated in Fig. 1b.

Here, lamellar colonies (LC) and γ grains (bright contrast) are easily distinguishable. The darkest parts marked $\beta_o(\omega_o)$ exhibit the so-called tweed contrast typical for the β_o-phase containing ω-type precipitates.

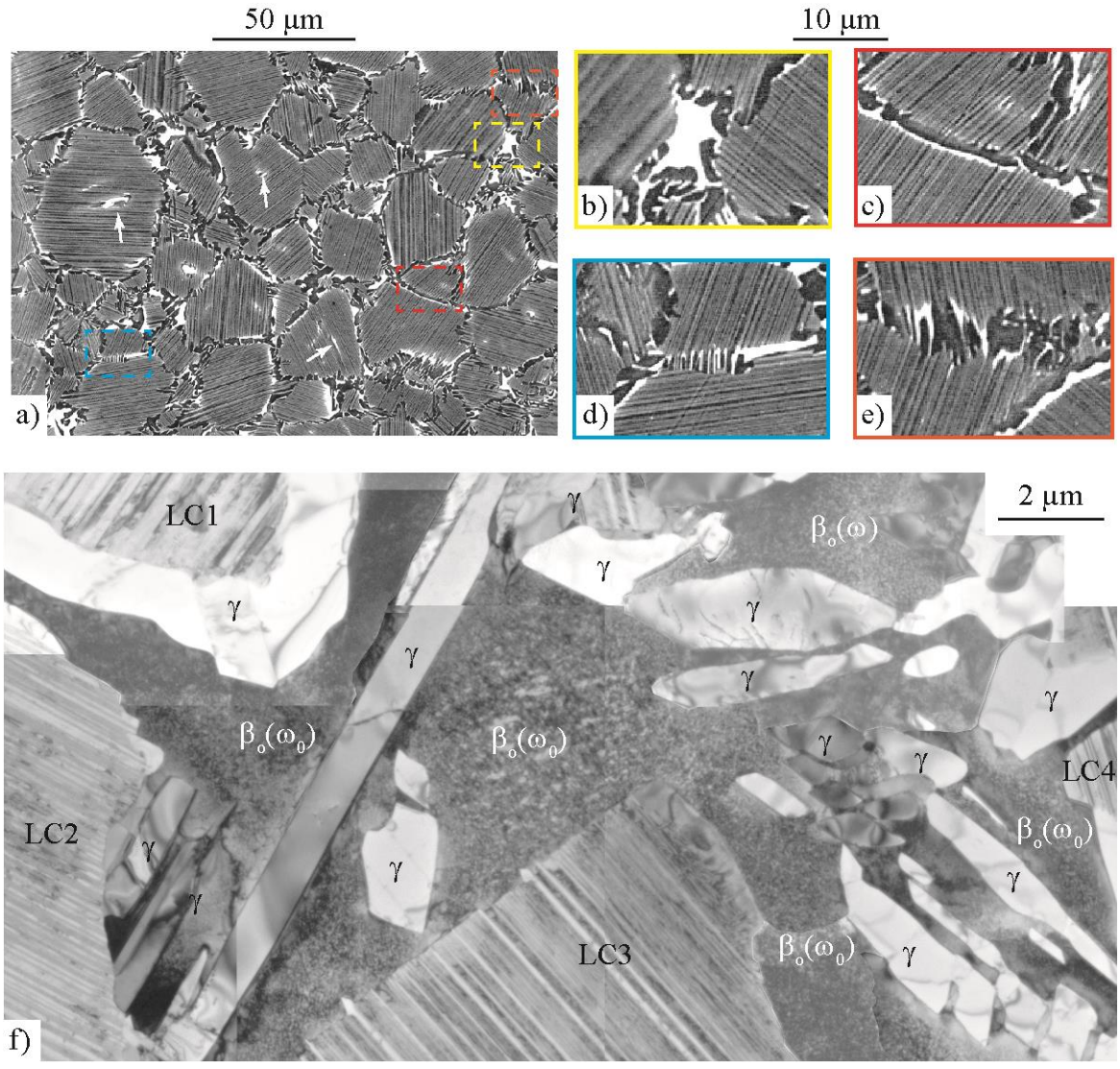

Fig. 1. *Microstructure of TNM-TiAl: (a) SEM micrograph of specimen AK746 taken in BSE mode with lamellar colonies surrounded by borders with γ and β_o grains in black and white colours, respectively. The four colour-framed micrographs correspond to four different enlargements displayed in (b), (c), (d) and (e) showing different distributions of the β_o phase (see text for details); (f) TEM micrograph of specimen AM504 with β_o phase distributed according to the situation imaged in Fig. 1b.*

Figure 2a depicts a diffraction pattern comparable to that previously reported for the bcc phases of conventional disordered Ti alloys [13,15,17,19] or intermetallic TiAl alloys. [10,11]. The β_o phase is oriented with a $<110>_{\beta o}$ direction of the zone axis parallel to the electron beam in this diagram, and the additional spots are due to the presence of two ω_0 variants. Looking at the $(\overline{222})_{\beta o}$ direction in particular, several spots are believed to originate from the variant for which the c axis is parallel to the $(\overline{222})_{\beta o}$ direction: one fundamental reflexion and two superstructure spots, resulting from the long range ordered structure. However, it may be argued that similar patterns have been seen in Ti and Zr alloys exhibiting a disordered β structure [13,15,17,19]. On the basis of image simulations, Sabeena [28] proposed that double diffraction explains the presence of these spots in a Ti-15Mo alloy.

Figure 2b depicts a dark field micrograph of a β_o area taken with $g=(0002)_{\omega o}$ superlattice diffraction vector, where the ω_o precipitates seem to have circular morphology. By counting the number of precipitates and determining the precipitates volume fraction, the ω_o precipitates are found to occupy a few volume percent (0.4 to 3.6 %) of the material and the order of magnitude of the distance between precipitates is about 27 nm (390 precipitates counted for one variant in a 182x394x434 nm^3 volume). Using the methods described in Ref. [29], a precise determination of the volume fraction, the precipitates size and spacing will be carried out in a forthcoming investigation. In addition, work is underway to determine the precise crystallographic structure of these ω_o precipitates, with a particular attention to their ordering state. Former studies have shown that the precipitation of ω_o phase requires either an ageing at intermediate temperatures, e.g. 700°C [10] or 850°C [21], or a slow cooling rate of 10 K/min [20]. This is consistent with our SPS experiments that exhibit cooling down from the dwell temperature (1300 °C or above, see Table 1) at a cooling rate of 100K/min inside the graphite mold maintained in the SPS set-up [25].

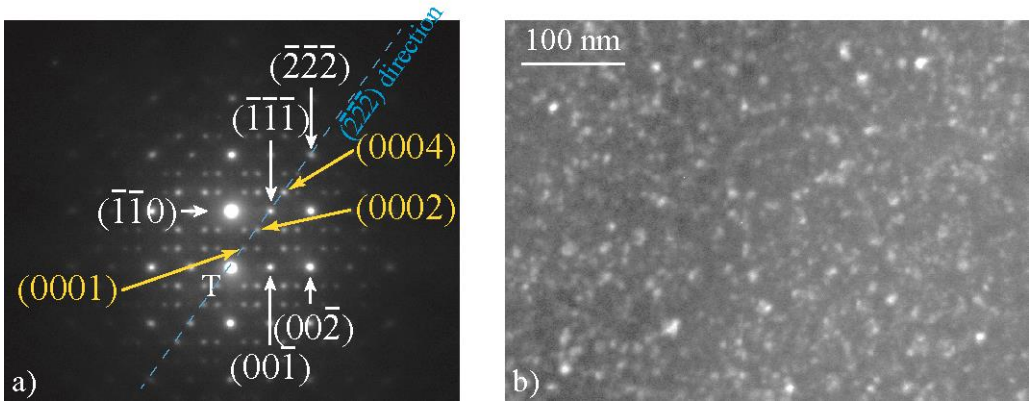

198

199 ***Fig. 2.*** *Characterization of the ω_o precipitates in β_o grains. a) Diffraction pattern with*
200 *<011>$_{\beta o}$ zone axis (the spots labelled in white correspond to the β_o phase; those labelled in*
201 *yellow to the ω_0 phase; the blue line indicates the $(\overline{222})_{\beta o}$ direction); b) Dark field micrograph*
202 *of the ω_0 precipitates taken with g=(0001)$_{\omega o}$ superlattice diffraction vector.*

203

204 **4. Mechanical tests and fracture surfaces**

205 The RT true stress vs. true strain curves (10^{-4} s^{-1} strain rate) are shown in Figure 3a for the four
206 SPS billets.

207 Yield stress (YS) is the stress at which plastic deformation starts and is defined as the stress at
208 10^{-3} % plastic elongation, $R_{0.2}$ denotes the tensile stress at 0.2 % plastic elongation, UTS the
209 ultimate tensile stress, and the term A represents the plastic elongation at rupture. As can be
210 seen in Table 2, the four billets exhibit similar mechanical properties. Indeed, as already
211 emphasized in as-SPSed B-containing TiAl alloys with the so-called GE composition (Ti-48Al-
212 2Cr-2Nb, in at.%) [30], as soon as the dwell temperature is situated in the single α or α+β phase
213 field, microstructures and mechanical properties are highly reproducible. The alloy densified at
214 1325 °C appears to have slightly improved properties resulting from a higher plastic elongation,
215 which leads to a higher ultimate tensile strength (UTS). This trend is not easily explained from
216 the measurements of the average grain size and of the volume fraction of β_o phase. Figure 3b

shows the curves obtained for four specimens extracted from two billets both densified at 1325°C (billets AK746 and AM797). These four samples exhibit very similar properties with reduced deviations on the different measured stresses (YS, R0.2, UTS) and on the plastic elongation at failure.

The plastic elongation at rupture for all hot-worked billets tested is between 0.5 and 1.0 %. As noted by Appel et al. [1], this limited RT ductility is typical for β-solidifying alloys, which possess a fairly high RT strength. However, using SPS as processing route appears to result in a slight increase in RT plastic elongation by generating uniform and non-textured microstructures.

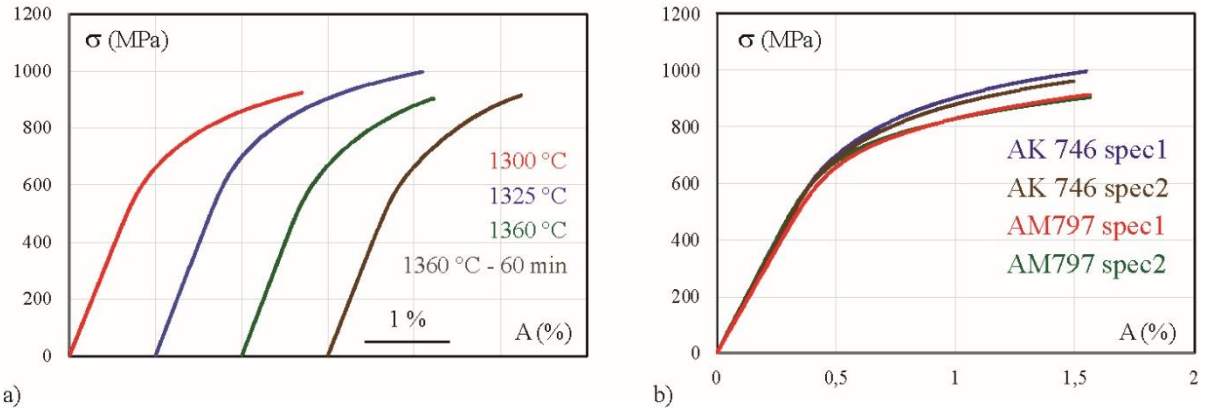

Fig. 3. *True RT stress-strain curves for the four investigated SPS treatments. (a) one curve for each condition; (b) four curves for the AK746 and AM797 specimens - 1325 °C dwell temperature (see Table 2 for details).*

238 **Table 2**

239 RT tensile tests results (10^{-4} s^{-1} strain rate).

Specimen name	Dwell temperature		YS (MPa)	$R_{0.2}$ (MPa)	UTS (MPa)	A (%)
AK 639	1300 °C	Spec 1	559	771	923	0.73
		Spec 2	554	759	910	0.75
AK 746	1325 °C	Spec 1	591	814	995	0.92
		Spec 2	583	792	961	0.81
AM797		Spec 1	559	755	914	0.93
		Spec 2	545	748	905	1
AL 824	1360 °C	Spec 1	538	770	901	0.54
AM 504	1360 °C - 60 min -	Spec 1	554	779	914	0.52
		Spec 2	528	763	880	0.44

240

241 A SEM study of the fracture surfaces is presented in Figure 4 for two RT deformed samples
242 (specimens AK 639 – Figs. 4a-b and AM504 - Figs. 45c-d, Table 2). Figure 4a shows
243 representative cleavage facets, the size of which matches that of lamellar colonies. The cleavage
244 is likely to occur along lamellar interfaces. Between these cleavage facets, transgranular crack
245 propagation is observed, as emphasized in Figure 4b showing at higher magnification some
246 steps between the cleaved planes, which might be in the γ lamellae. The micrographs in Fig. 4c
247 and Fig. 4d depict an area both in backscattered mode and by a Mo EDX SEM map,
248 respectively. The β_o phase is indicated by the bright yellow regions. This demonstrates that the
249 β_o areas do not show any particular brittle behaviour.

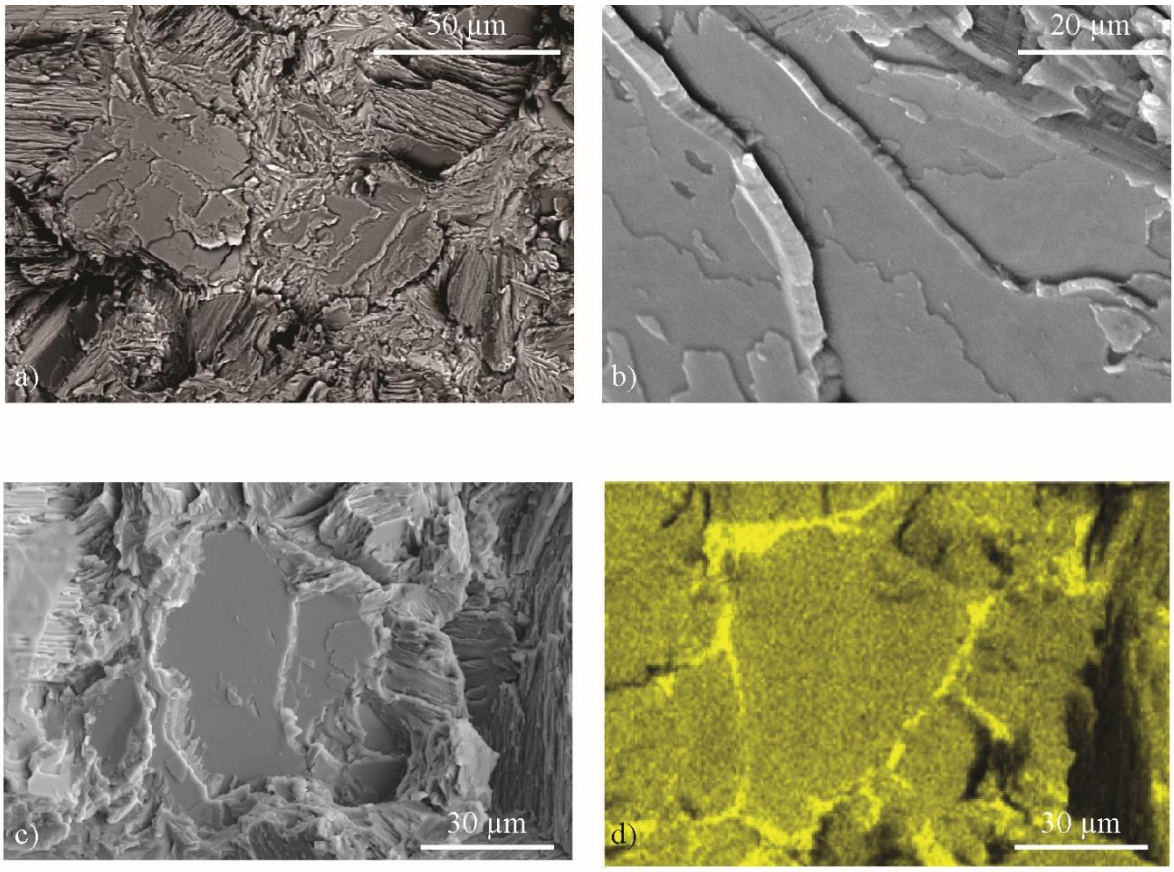

Fig. 4. *SEM characterization of the fracture surface of RT deformed samples until rupture (AK 639 – Figs. 4a-b and AM504 - Figs. 4c-d, Table 2). (a) and (b) fracture surfaces; (c) and (d) same area in BSE mode and as a Mo EDX SEM map, respectively.*

5. Study of the deformation processes for β_o grains

Characterization of the deformation processes operating in β_o grains was carried out by both TEM post-mortem analyses of thin foils extracted from RT deformed samples until rupture (specimen AM 504, Table 2) and TEM in-situ straining experiments in samples cut from the same AM 504 billet.

5.1. Dislocation microstructure in deformed samples

About fifteen grains were examined by TEM and the presence of dislocations was observed in most of them (Figures 5 and 6). On the general view (Fig. 5a), several groups of dislocations are observed. As shown in the two inserts (Figs. 5b and c), dislocations are out of contrast with the $(0\bar{1}1)$ and $(\bar{1}01)$ reflexions demonstrating that their Burgers vector is parallel to the [111] direction, as this is the case for every dislocations in this area (circled detail labelled F serves as a mark in Figs. 5a-c). Dislocations are generally organized in pile-ups, where traces on the thin foil surfaces permit to determine their glide plane. For the pile-up of three dislocations (marked A, Fig. 5a), the trace is parallel to the $(\bar{1}01)$ plane. A tilt experiment (not reproduced here), for which this pile-up was observed at different inclinations tilted around this trace has clearly confirmed that it is located in the mentioned $(\bar{1}01)$ plane, which is a glide plane for these [111] dislocations. This is also the case for the pair of dislocations marked B. The trace of the main pile-up marked C is not straight but curved (see dashed line) indicating changes in the glide plane. The analysis of the surrounding γ grains showed that these pile-ups can be associated with the locking of a twin on the grain boundary, as in case D, or not, as in the case of pile-up C. Hence, Fig. 5d confirms the strong influence of the deformation occurring in the γ phase on that proceeding in the β_o phase. In this area, three parallel noodle-shaped β_o grains are situated within one γ grain deformed by twins. Clearly, some dislocations are seen in the noodle-shaped constituents in planes following those of the twin habit planes, thus indicating that the emission of dislocations in the β_o phase results from the transmission of deformation from surrounding γ phase.

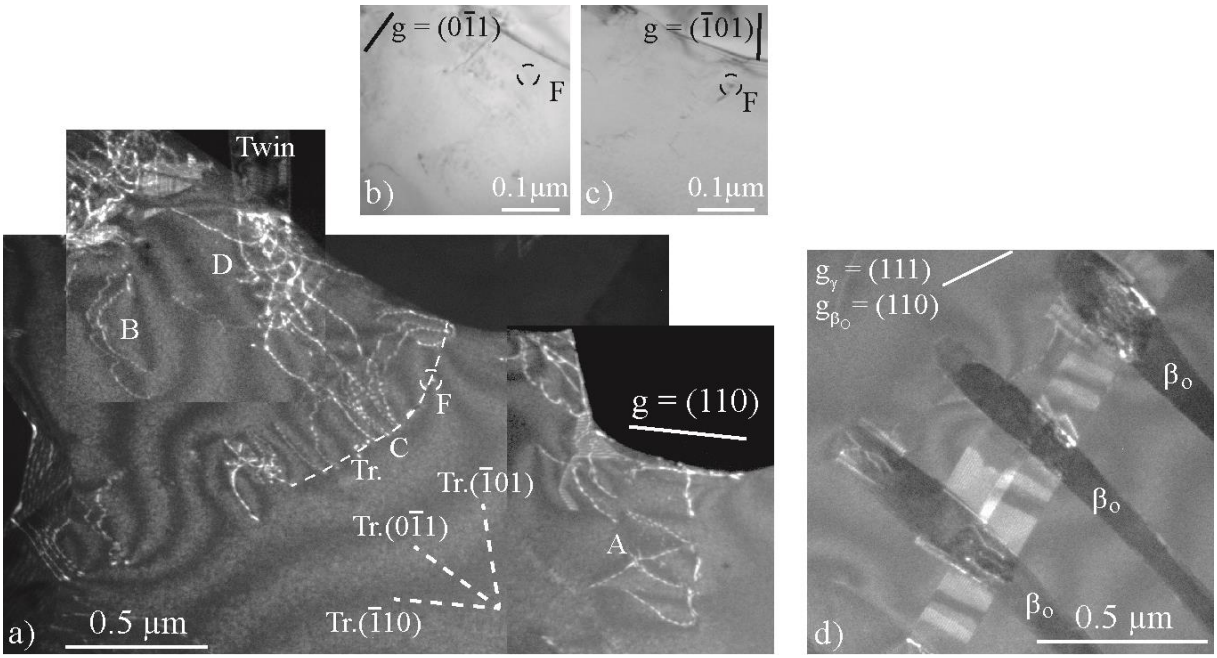

283

284 ***Fig. 5.*** *Characteristic occurrence of dislocations observed by TEM (weak-beam conditions) in*
285 *a sample macroscopically strained until rupture (AM504, Table 2); (a) general view; (b) and*
286 *(c) same dislocations out of contrast under two imaging conditions; (d) three parallel noodle-*
287 *shaped β_o phase containing some dislocations inside a γ grain deformed by mechanical twins.*

288

289 Figure 6, which is taken under higher magnification, gives two examples of the structure of
290 these <111> dislocations. In Fig. 6a, dislocations are localized in a pile-up, whereas Fig. 6b
291 shows an isolated long dislocation, the rectilinear segments of which are parallel to the screw
292 direction of the dislocation. Dislocations are often pinned at small obstacles, as indicated by
293 small white arrows in Fig. 6a. Every dislocations clearly appear as paired dislocations in every
294 cases but with notable differences in spacing. In particular in the pile-up, various spacing is
295 likely to occur from the presence of pinning points (arrowed). Without pinning points, the
296 spacing of paired dislocations is approximately constant all along the line with an apparent
297 value (d_a) ranging from 5 to 10 nm. The long dislocation also exhibits macrokinks, which are
298 reminiscent of the dislocation structures in $L1_2$ intermetallic compounds such as Ni_3Al and

299 Ni_3Ga [31, 32]. It is even tempting to underline an alignment of the leading and trailing partials
300 bordering a macrokink as evidenced in Ni_3Al and Ni_3Ga alloys deformed at RT [31, 33] as the
301 result of jump amplitudes equal to the width of the antiphase boundary separating the two
302 superpartial dislocations of the a<011> dislocations involved in these face-centered cubic type
303 intermetallic alloys.

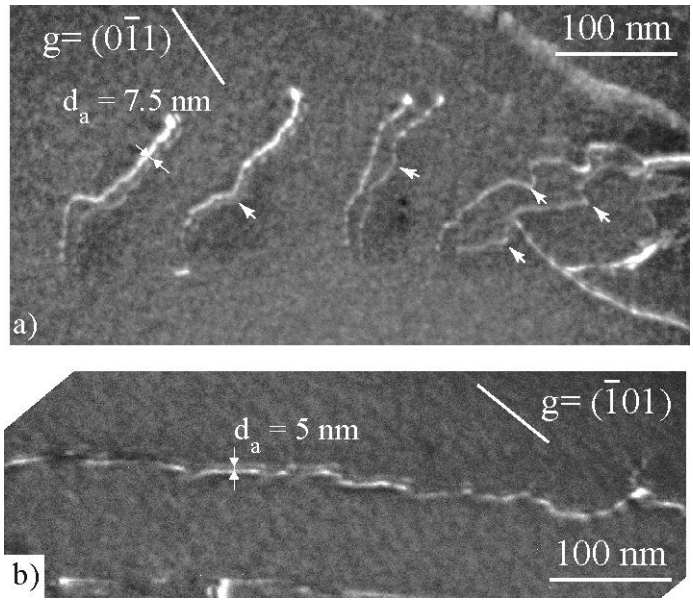

304

305 ***Fig. 6.*** *Two examples of the structure of a<111> superdislocations observed by post-mortem*
306 *TEM under weak-beam conditions (AM504). (a) dislocations localized in a pile-up; (b) isolated*
307 *dislocation.* d_a *corresponds to the apparent average distance between superpartial*
308 *dislocations.*

309

310 The obtained experimental results can be interpreted as follows:

311 • a<111> dislocations are dissociated into two identical dislocations bordering an
312 antiphase boundary (APB), consistently with the following dissociation scheme:

313 $$a\langle 111\rangle \rightarrow a/2\langle 111\rangle + APB + a/2\langle 111\rangle$$

(as the lengths of the Burgers vectors of these a/2<111> partial dislocations and a<111> dislocations result from the long range ordered structure, they are generally called superpartial dislocations and superdislocations).

- Dislocations are often confined in pile-ups, gliding in {110} type planes.
- Assuming that the APB ribbon lays in the gliding plane, a dissociation width ranging from 10 to 20 nm can be deduced from the apparent dissociation distances measured on the rectilinear dissociated dislocation segments.
- Extrinsic obstacles pin superpartial dislocations, leading to a wide range of dissociation distances of the superdislocations.

5.2. In-situ observation of the movement of a<111> dislocations in β_o grains

The movement under stress of these a<111> dislocations was studied by performing in-situ RT straining experiments in a TEM (note that Figs. 7-10 were made from the video sequences available for each figure; it is worth noting that these sequences are at real speed). The main tendency of these dislocations is to move in pile-ups as illustrated by Fig. 7 (video **here**), where a small defect, labelled F, is used as a reference point. In Fig. 7a, three dislocations (labelled d1, d2 and d3) with a a[111] Burgers vector are visible. They have left slip traces behind them (marked by white triangles) in the form of weak contrasted lines on the two thin foil surfaces. The determination of the grain orientation through a stereographic analysis has shown that these traces are parallel to the $(\bar{1}10)$ plane containing the a[111] Burgers vector. With elapsing time (Fig. 7b), d1 and d2 have glided on upward in this plane and a lot of dislocations are now present in a pile-up created in the wake of d1 (each bright dot on the upper trace of the pile-up indicates the presence of one gliding dislocation; the dashed oval surrounded some of these dots). In this figure, the pile-up tip is visible in the observed area and a dislocation loop (arrowed) was formed due to the pinning of one dislocation. Between Fig. 7b and Fig. 7c, d1 has moved on, followed

by the pile-up. In Fig 7c, the pile-up tip is out of the frame and the dashed oval shows some twenty dots/piled-up dislocations. The dynamic sequence allows claiming that several hundreds of dislocations glided in the β_o grain in a few seconds following the path of dislocation d1.

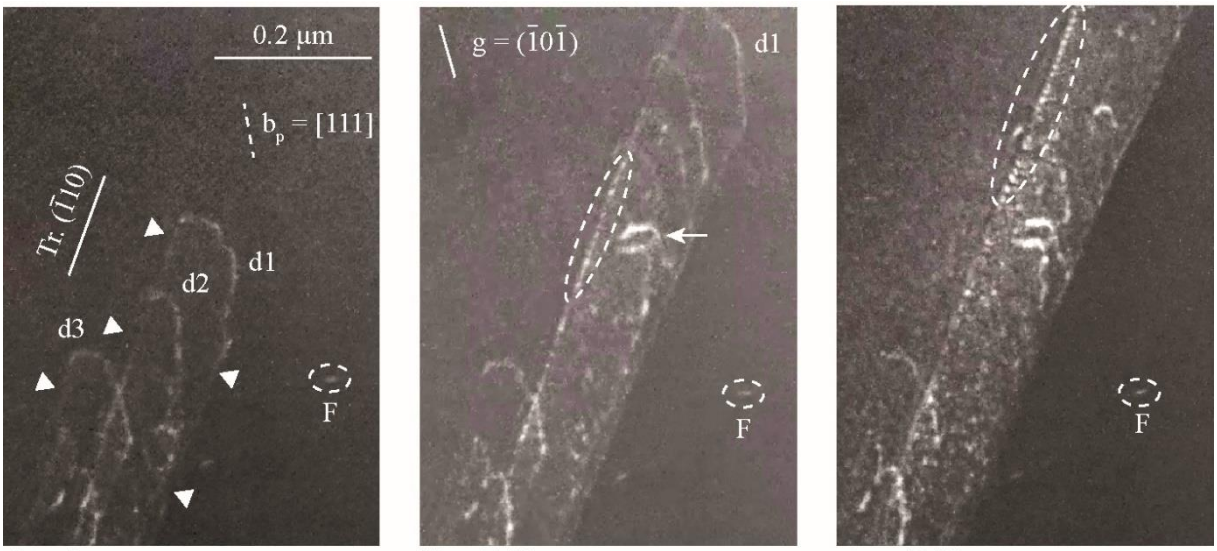

a) t= 0 s b) t= 7.54 s c) t= 40.57 s

Fig. 7. *Formation of a* $(\bar{1}10)$ *pile-up of a[111] dislocations during an in-situ RT straining experiment in a TEM (see corresponding video sequence and text for more details). (a) initial situation with dislocations d1, d2 and d3 (*b_P *direction corresponds to the projected direction of the [111] Burgers vector on the image plane); (b) creation of the pile-up in the wake of dislocation d1; (c) progress of the pile-up made of hundreds of dislocations.*

Figure 8 details the elementary mechanisms of propagation of these dislocations. Figures 8a-c (video **here**) depict another pile-up generated in the same grain as shown in Fig. 7, whereas Figs. 8d-f show the situation in another sample. Figs. 8a-c show a pile-up tip, where dislocations appear dissociated according to the dissociation mode analysed in section 5.1 (F is a reference point). In this area, the pile-up tip is made of three superdislocations (Figs. 8a-b) joined later on by a fourth one (Fig. 8c). It can be seen that the spacing between the two superpartials of a given superdislocation is increased with the distance of the considered superdislocation from

the pile-up tip (in Fig. 8a, dislocation d4 is more widely dissociated than dislocation d2, for example), as that was observed in the bulk (Fig. 6a). The spacing between the two superpartial dislocations of leading dislocation d1 is even difficult to observe due to the resolution limit of this micrograph. Between Fig. 8a and Fig. 8b, however, all three dislocations have moved on. Examination of the video shows that these dissociated superdislocations move in a jerky manner, mainly by independent jumps of the superpartials. Figs. 8d-f (video **here**) follow the movement of another a<111> superdislocation in a different grain, which is not strictly speaking part of a pile-up even though several other dislocations are simultaneously active in the same area. In this case, imaging conditions did not allow the right resolution to be achieved for visible dislocation dissociations. Dislocations are elongated along their screw orientation and anchored at many pinning points (some of them are indicated by small triangles on two dislocations visible in the frame corresponding to Fig. 8e). A dislocation marked D is followed between frame 1 (D1 in Fig. 8d) and frame 3 (D3 in Fig. 8f, 1 minute later). The whole dislocation jumps between positions D1 and D2 between frames Fig. 8d and Fig. 8e (dashed circled small defect is a fixed spatial reference). In position D2, the dislocation is divided into two segments separated by a pinning point (marked PP). Subsequently, probably due to the higher strength of this pinning point, dislocation D splits into two segments that move independently by the same jerky motion (Fig. 8e), leading to the formation and expansion of a loop.

From these images, it is possible to estimate the distance between the pinning points anchoring these moving a<111> screw dislocations: the apparent distance D_{AP} is about 30 nm (distance D_{AP} plotted on frame Fig. 8e), which corresponds to a true distance of 35 nm considering the inclination of the screw dislocation line. This order of magnitude is compatible with the apparent distance between ω_o precipitates (see Fig. 2b), thereby confirming that dislocation anchoring occurs on these ω_o precipitates.

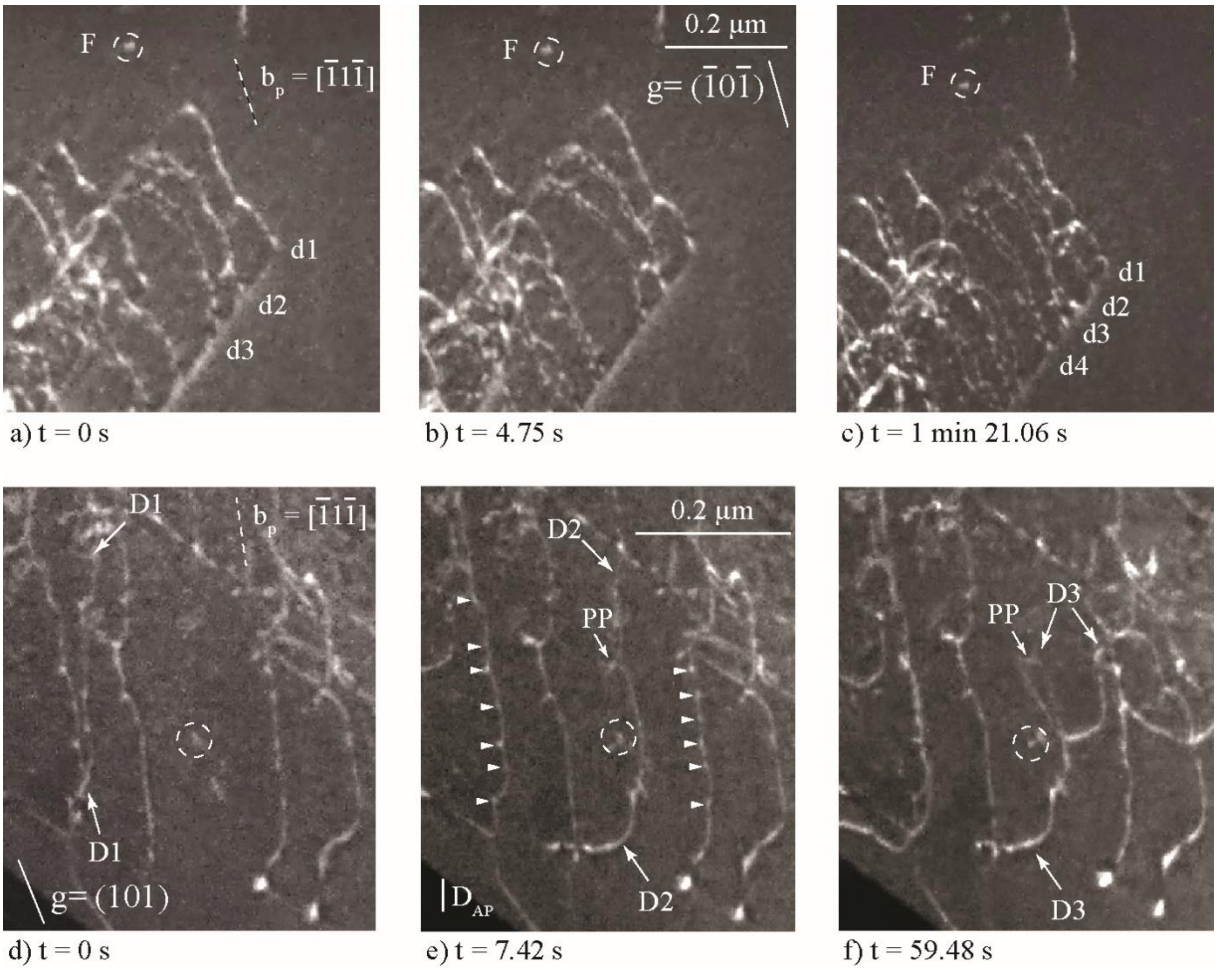

381

382 ***Fig. 8.*** *Propagation of a<111> superdislocations in β_o grains during in-situ RT straining*
383 *experiments in a TEM (see corresponding video sequence and text for more details). Figs. 8a-*
384 *c depict dislocations of a pile-up generated in the same grain shown in Fig. 8; Figs. 8d-f are*
385 *imaging isolated dislocations in another grain of another thin TEM foil.*

386

387 **6. Investigation of the cracking process by in-situ straining experiment**

388 In the β_o grain, where the sequence shown in Fig. 7 was taken, four pile-ups were in fact
389 observed in almost parallel planes. Figs. 9a-d (video **here**) present the evolution of one of them
390 labelled PU in Fig. 9a. The dislocations moved upwards in the observed area and Fig. 9a is a
391 first micrograph of the area when PU already reached the grain boundary labelled GB located
392 at the upper part of the micrograph. The rest of the dynamic sequence was recorded inside the

β_o grain ('below' GB). Between Figs. 9b and c, the apparent width of PU decreases with the accumulation of new dislocations in the pile-up. This effect is due to the relative slip of the respective part of the grain located on both sides of pile-up PU. Suddenly, the grain cracked at the level of the pile-up, see Fig. 9d. Regarding Fig. 9e, it shows a β_o grain characterized by post-mortem TEM in a thin foil extracted from a RT tensile specimen. The pile-up labelled PU, evidenced in Fig. 9e, demonstrates that localization of deformation in the form of large pile-ups (in addition to the small pile-ups already mentioned in Figs. 5 and 6) is also possible in the bulk and not limited to in-situ tests in thin specimens.

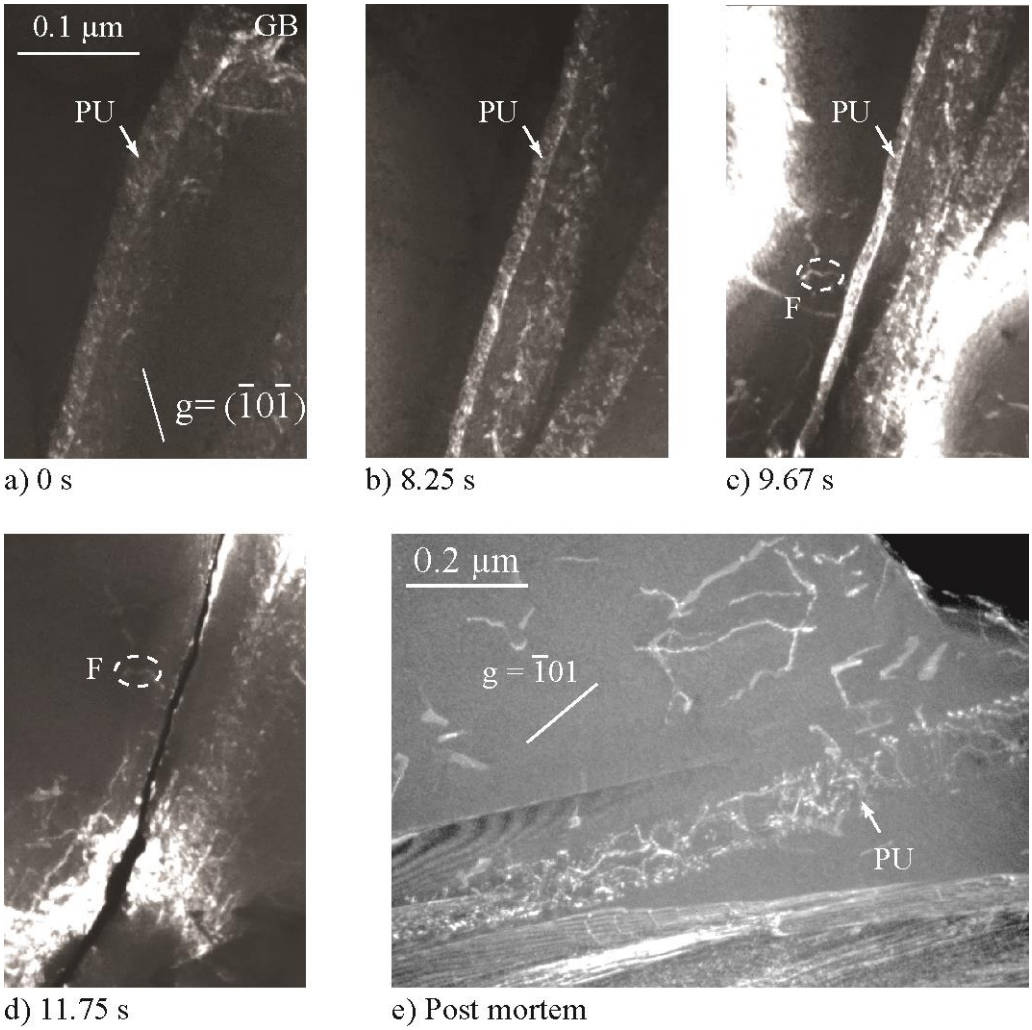

Fig. 9. *Pile-up growing and crack formation in a β_o grain; (a-d) dynamics of a growing pile-up leading to the nucleation of a crack (in-situ TEM; see corresponding video sequence and*

text for more details); (e) pile-up of the same nature observed by post-mortem TEM conducted in a foil taken from tensile test specimen.

7. Discussion

The present TEM studies have shown that the β_o phase can be plastically deformed at RT by dislocations, consistently with the work of Morris et al. [5, 6]. It is recalled that these authors investigated a Ti-44Al-2Mo (at%) alloy and observed a<111> and a<001> dislocations presumably nucleated in β_o grains by the local stress generated on the grain boundaries by mechanical twins emitted in neighbouring γ grains. In the present work, deformation is shown to occur by a<111> superlattice dislocations, which are often situated in pile-ups. Some evidences of deformation in β_o areas originated by twins in γ grains have also been observed (Fig. 5). Not shown here, other families of dislocations have also been observed and are currently under investigation. Many of the features of these a<111> superlattice dislocations are reminiscent of observations previously obtained for deformation systems active in other intermetallic compounds (ordinary dislocations in the γ phase of TiAl, superlattice dislocations in $L1_2$ (Ni_3Al and Ni_3Ga) and $D0_{19}$ structures (Ti_3Al)):

- The dissociation scheme determined in section 5.1 is the one expected from the literature concerning intermetallic alloys with B2 structure [34], even though in NiAl B2-type intermetallic alloys the core of these dislocations has been found to be very compact by TEM [35, 36]. These superlattice dislocations are dissociated into two identical superpartials bordering an antiphase boundary ribbon as in Ni_3Al [31, 32] and Ni_3Ga [33], both with the $L1_2$ fcc-type ordered structure, and also in α_2-Ti_3Al [37]. Superpartials exhibit superkinks, each of them resulting of a dislocation elementary jump.

- The dislocations are elongated along their screw directions, with sometimes some rectilinear parts for the superpartials, as observed in Ni_3Al and Ni_3Ga, as well as during the prismatic glide in α_2-Ti_3Al. This is generally explained by a superpartial core spreading out of the glide plane, which leads to a lattice friction stress (Peierls stress), thus hindering dislocation glide.
- Dislocations glide is made of quick jumps (in less than the time between two successive video frames i.e. 1/50 s) between two elongated screw configurations. This jerky motion is also the result of the lattice friction stress [38]. Indeed, dislocations transit from a stable sessile configuration due to the core spreading, to a non-stable glissile configuration allowed by the thermally activated recombination of the core under the effect of the local stress, before again falling in the stable configuration.
- Dislocations are anchored at pinning points, which are ω_o precipitates. This situation is analogous to that of ordinary dislocations in the γ TiAl phase [39-41], in which the pinning was attributed to small chemical clusters [42], but also to the case of precipitation hardened Al base alloys [43], in which dislocations anchor on precipitates made of crystallographic phases different from that of the matrix.
- Loops formation leading to dislocation multiplication processes are often observed. These mechanisms are frequently evidenced when extrinsically pinned dislocations are subjected to friction forces: their screw character induced by the Peierls stress allows intense cross-slip events, in a similar manner as ordinary dislocations in TiAl [39-41].

Regarding the β_o phase present in the investigated TNM-TiAl alloy, a<111> superdislocations experience a friction force and must overcome the ω_o precipitates in order to continue gliding, precisely in the {110} planes, the densest planes of the B2 structure. The tendency for these dislocations to align along their screw direction is less marked than in other intermetallic alloys, especially by considering whole dislocations (Figs. 8 d-f). Sometimes, this alignment seems to

be more pronounced for partial dislocations (Figs. 8 a-c). On the other hand, the anchoring points are very close with a separation distance of the order of 35 nm smaller than that measured for ordinary dislocations in the TiAl γ-phase (150 nm [41, 42]). On the reverse, this distance is close to that separating the precipitates of Al alloys (30 nm) [43], in which the structural hardening due to these precipitates is known to control deformation. This suggests that ω_o precipitates have a dominant role here on the dislocations mobility.

Furthermore, the trend of having dislocations moving in pile-ups with a tendency for decorrelation of the superpartials, provides a strong evidence ev that superdislocations are far from the pile-up tip, as been observed during in-situ straining experiments. It is tempting to conclude that this pile-up effect results from the structure of the ω_o precipitates which are crossed by dislocations. An analogous situation is found in the short-range order effect detected in the γ-phase of Ni base superalloys [44], where the formation of pile-ups results from the greater facility of dislocations to move in the wake of the head dislocations once the ordered structure has been sheared. To check the key role of ω_o precipitates on the formation of dislocations pile-ups , a specific TEM in-situ RT experiment was carried out in β_o grains of a Ti-44Al-3Mo alloy (at. %) characterized by the absence of ω_o precipitates due to the absence of Nb. As shown in Fig. 10 (video **here**), dislocations observed in the starting situation (Fig. 10a) have been progressively emitted in the β_o grain from a grain boundary situated out of the frame on the right side of the picture. Dislocations are spread all over the area. The extremity of a dislocation marked by the letter F which will not move anymore is used as a reference point in the next three images. An indexation of these dislocations allowed us to determine that their Burgers vector is parallel to the <111> crystallographic direction and to deduce that these dislocations have a marked screw character. A TEM analysis under weak-beam conditions, which is not reproduced here, showed that these dislocations are dissociated into two partials separated by an APB ribbon of the order of 7 nm on screw segments. Regarding the dynamics

of these dislocations, Figs. 10b-d allow to follow the path of a dislocation indicated by an arrow: this dislocation occurs in the observed area (Fig. 10b) and moves individually to position indicated in Fig. 10.c, until reaching the position indicated in Fig. 10.d. The trace left on the surface corresponds to a (101) gliding plane. Dislocations activated in the β_o phase of this material with no ω_o precipitates are therefore similar to the dislocations investigated in the β_o phase of the TNM alloys with ω_o precipitates, but keeping in mind that they move individually without forming pile-ups. It is worth noting that even if it would be interesting to carry out mechanical tests to determine the mechanical impact of the absence of ω_o precipitates, we did not do so: a fair comparison with the TNM alloys would indeed require the manufacturing of a material with a similar microstructure. This is really a long and difficult task including atomization of the right pre-alloyed powder, SPS densification etc, that is out of the scope of this work.

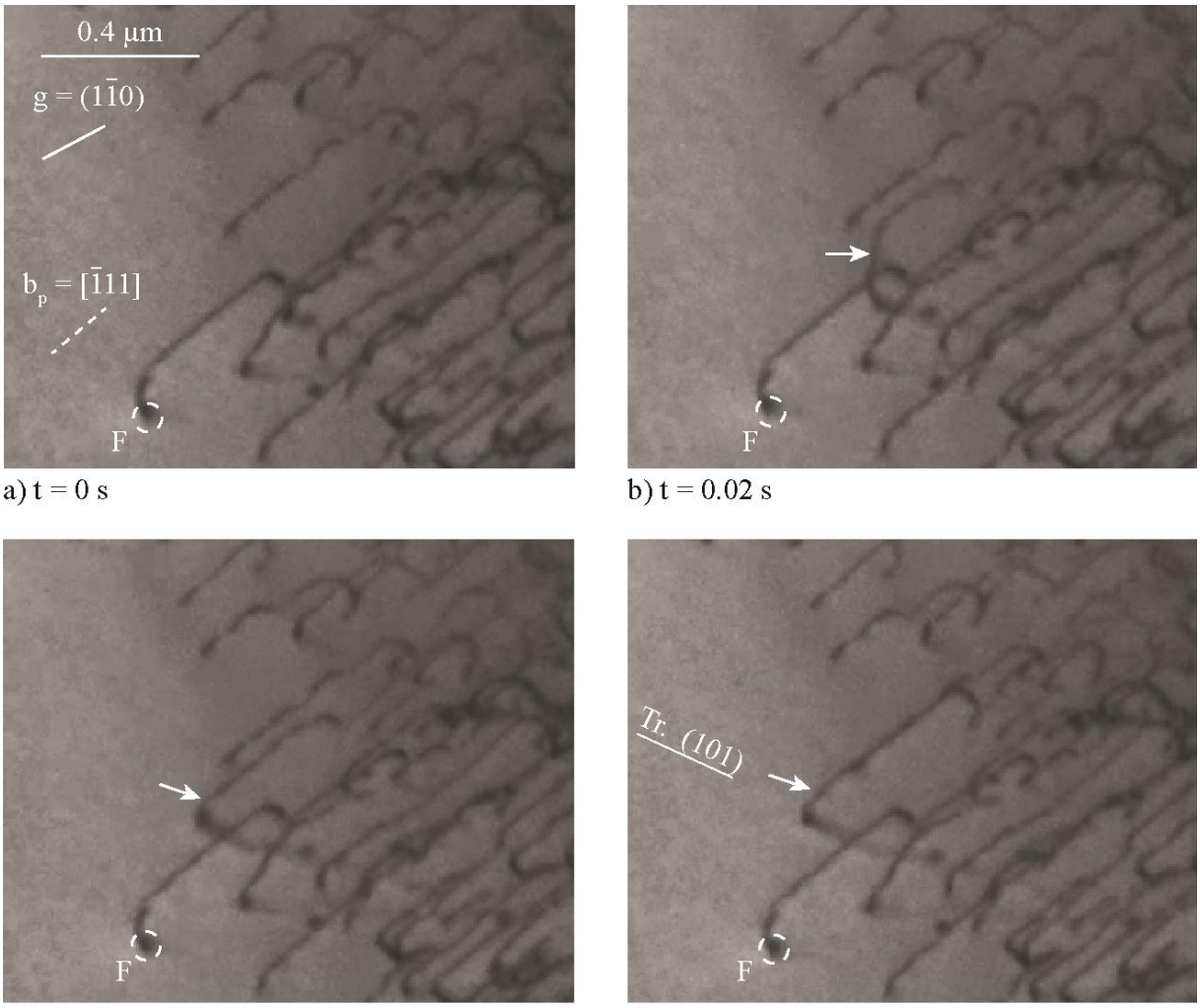

490

491 ***Fig. 10.*** *Propagation of a<111> superdislocations in a β_o grain with no ω_o precipitates during*
492 *an in-situ RT straining experiment in a TEM; (a) starting situation with the extremity of*
493 *dislocation used as a reference point; (b-d) arriving and propagation of a dislocation*
494 *(arrowed).*

495 In summary, the movement of a<111> dislocations and the formation of corresponding pile-
496 ups appear to result from the presence of ω_o nanoprecipitates that seem to play a key role in the
497 dynamics of the dislocations involved. It should be noted that further information is needed to
498 fully understand the glide mechanism of these dislocations. Work is currently in progress to
499 obtain quantitative results on that particular topic.

This experimental study did not reveal any particularly brittle behaviour of the β_o phase since we did observe deformation dislocations and no brittle rupture surface. On the other hand, we evidenced a strong tendency to form pile-ups of large numbers of dislocations. Even though pile-ups are enhanced by in-situ experiments, however, it is worthwhile pointing out that a pile-up of the same type has been found in a post-mortem sample and pile-ups made of few dislocations, probably embryos of large pile-ups, were also evidenced. As failure is linked to a localised event that does not necessarily need to occur many times in the material, it can be assumed that the occurrence of only a few pile-ups in the bulk material (or even just one if it is well oriented with respect to the neighbouring lamellar colony) is sufficient to induce failure of the TiAl alloy. These pile-ups contain many dislocations, involving high stress concentrations that can lead to the cleavage along a lamellar interface if the lamellar colony is well oriented. Consistently with the limited slip activity of the α_2 phase [5, 6] and with the observation of intensive cleavage in lamellar interfaces, the low ductility of the present alloy is thus attributed to a stress mediated cleavage process along lamellar interfaces. As Tables 1 and 2 show, beyond a few microns (around 20 μm) the size of the lamellar colonies has no additional detrimental effect on fracture (A= 0.5 %) because the surface of the cleaved interface certainly exceeds the critical size for an irreversible failure. Similarly, the proportion of β_o phase has little influence since the fracture results from a localised process in the material and not from the average deformation of the β_o phase. However, only a certain volume fraction of β_o phase is required to make the stress concentration possible in some sites.

8. Conclusion

The deformation microstructure and the fracture surface have been studied in a TNM-TiAl alloy ($Ti_{51.05}Al_{43.9}Nb_4Mo_{0.95}B_{0.1}$) densified by Spark Plasma Sintering. RT tensile tests were coupled

with TEM in-situ RT straining experiments. A cleavage mechanism was observed in the lamellar interfaces of the γ/α_2 colonies but not in the β_o grains. The latter were found to be plastically deformable by a<111> superlattice dislocations, which are dissociated into two superpartials separated by an antiphase boundary. These dislocations mainly glide in pile-ups lying in {110} planes and involving many dislocations. In addition, the β_o phase contains ω_o nanoprecipitates, which anchor the dislocations, thus limiting their propagation and enhancing pile-ups configurations.

In summary, this study shows that fracture of β_o-containing TiAl alloys occurs by cleavage along the interface plane of the lamellar γ/α_2 colonies, in a similar manner as in lamellar TiAl alloys with no β_o phase. However, this cleavage mechanism is premature since ω_o precipitates that are present in the β_o phase, as a result of Nb addition in the TNM alloy, promote stress concentrations by the formation of dislocation pile-ups in this phase. Therefore, such dislocation pile-ups are believed to trigger cleavage in the neigbouring lamellar colonies.

Acknowledgements

This study has been conducted in the framework of the cooperative Austrian-French project "Hi-TiAl - 18-CE91-0008-01" co-supported by the French Agence Nationale de la Recherche (ANR) and the Fonds zur Förderung der wissenschaftlichen Forschung (FWF).

This project has received funding from the European Union's Horizon 2020 research and innovation programme under grant agreement No 823717 – ESTEEM3.

546 **References**

547 [1] F. Appel, J. Paul, M. Oehring: *Gamma Titanium Aluminides: Science and Technology, ©*
548 *Wiley-VCH Verlag GmbH &Co. KGaA*, 2011.

549 [2] R. Hoppe, F. Appel, Acta Mat., Deformation-induced internal stresses in multiphase
550 titanium aluminide alloys, Acta Mat., 64 (2014) 169-178.

551 [3] P. Erdely, P. Staron, E. Maawad, N. Schell, H. Clemens, S. Mayer, Lattice and phase strain
552 evolution during tensile loading of an intermetallic, multi-phase γ-TiAl based, alloy, Acta Mat.,
553 158 (2018) 193-205.

554 [4] F.S. Sun, C.X Cao, S.E. Kim, Y.T. Lee, and M.G. Yan, Alloying Mechanism of Beta
555 Stabilizers in a TiAl Alloy, Metallurgical and Materials Transactions 32A, 10 (2001) 1573-
556 1589.

557 [5] M.A. Morris, Y.G. Li, Deformation mechanisms and slip transfer in a Ti-44Al-2Mo alloy,
558 Materials Science and Engineering A 197 (1995) 133-145.

559 [6] M.A. Morris, Y.G. Li, Deformation mechanisms within the B_2, $L1_0$ and DO_{19} structures of
560 a Ti-44Al-2Mo alloy, Gamma Titanium Aluminides, Edited by Y.W. Kim, R. Wagner and M.
561 Yamaguchi, The Mineral, Metals and Materials Society, (1995), 353-361.

562 [7] T. Leitner, M. Schloffer, S. Mayer., J. EβLinger, H. Clemens, R. Pippan, Fracture and R-
563 curve behavior of an intermetallic β-stabilized TiAl alloy with different nearly lamellar
564 microstructures, Intermetallics, 53 (2014) 1-9.

565 [8] H. Clemens, Wallgram W, Kremmer S, Güther V, Otto A, Bartels A, Design of Novel β-
566 Solidifying TiAl Alloys with Adjustable β/B2-Phase Fraction and Excellent Hot-Workability,
567 Adv. Eng. Mater. 2008;10: 707.

568 [9] S. Mayer, P. Erdely, F.D. Fischer, D. Holec, M. Kastenhuber, T. Klein, H. Clemens,
569 Intermetallic β-solidifying γ-TiAl based alloys: from fundamental research to application, Adv.
570 Eng. Mater. 19-4 (2017) 1–27.

571 [10] L.A. Bendersky, W.J. Boettinger, B.P. Burton, F.S. Biancaniello, The formation of the
572 ordered ω-related phases in alloys of composition Ti_4Al_3Nb, Acta Metall. Mater., 38 (1990)
573 931-943.

574 [11] W. Wallgram, T. Schmölzer, L. Cha, G. Das, V. Güther, H. Clemens, Technology and
575 mechanical properties of advanced γ–TiAl based alloys, Int. J. Mat. Res., 100 (2009) 1021-
576 1029

577 [12] J.M. Silcock, An X-ray examination of the ω phase in TiV, TiMo and TiCr alloys, Acta
578 Metallurgica, 6 (1958) 481-493.

579 [13] D. de Fontaine, N.E. Paton, J.C. Williams, The omega phase transformation in Titanium
580 alloys as an example of displacement controlled reactions, Acta Metallurgica, 19 (1971) 1153-
581 1162.

582 [14] F. Prima, P. Vermaut, G. Texier, D. Ansel, T. Gloriant, Evidence of a-nanophase
583 heterogeneous nucleation from w particles in a b-metastable Ti-based alloy by high-resolution
584 electron microscopy, Scripta Materiala, 54 (2006) 645-648.

585 [15] A. Devaraj, S. Nag, R. Srinivasan, R.E.A. Williams, S. Banerjee, R. Banerjee,

586 H.L. Fraser, Experimental evidence of concurrent compositional and structural instabilities
587 leading to x precipitation in titanium–molybdenum alloys, Acta Materiala, 60 (2012) 596-609.

588 [16] J Smilauerova, P. Harcuba, D. Kriegner, V. Holy, On the completeness of the β → ω
589 transformation in metastable β titanium alloys, J. Appl. Cryst., 50 (2017) 283-287

590 [17] J. Ballor, T. Li, F. Prima, C.J. Boehlert, A. Devaraj, A review of the metastable omega
591 phase in beta titanium alloys: the phase transformation mechanisms and its effect on mechanical
592 properties, International Materials Reviews, DOI:10.1080/09506608.2022.2036401 (2022)

593 [18] Banerjee S, Mukhopadhyay P. Phase transformations: examples from titanium and
594 zirconium alloys. Oxford: Pergamon Press; 2004]

595 [19] S. Banerjee, R. Tewari, G.K. Dey, Omega phase transformation – morphologies and
596 mechanisms, Int. J. Mat. Res. 97 (2006) 963-977.

597 [20] A. Stark, M. Oehring, F. Pyczak M, A. Schreyer, In Situ Observation of Various Phase
598 Transformation Paths in Nb-Rich TiAl Alloys during Quenching with Different Rates, Adv.
599 Eng. Mater. 13-8 (2011) 700–704.

600 [21] M. Schloffer, B. Rashkova, T. Schöber, E. Schwaighofer, Z. Zhang, H. Clemens, S. Mayer,
601 Evolution of the ω_o phase in a β-stabilized multi-phase TiAl alloy and its effect on hardness,
602 Acta Metall. Mater., 64 (2014) 241-252.

603 [22] X. Wang, J. Yang, K. Zhang, R. Hu, L. Song, H. Fu, Atomic-scale observations of B2→
604 ω-related phases transition in high-Nb containing TiAl alloy, Materials Characterization, 130
605 (2017) 135-138.

606 [23] T. Klein, M. Schachermayer, D. Holec, B. Rashkova, H. Clemens, S. Mayer, Impact of Mo
607 on the ω_0 phase in β-solidifying TiAl alloys: An experimental and computational approach,
608 Intermetallics, 85 (2017) 26-33.

609 [24] R. Gerling, H. Clemens, FP. Schimansky, Power metallurgical processing of intermetallic
610 gamma titanium aluminides, Adv. Eng. Mater. 6-1 (2004) 23-38.

611 [25] T. Voisin, L. Durand, N. Karnatak, S. Le Gallet, M. Thomas, Y. Le Berre, J.F. Castagne,
612 A. Couret A, Temperature control during Spark Plasma Sintering and application to up-scaling
613 and complex shaping, Journal of Materials Processing Technology, 213 (2013) 269-278.

614 [26] T. Voisin, J.P. Monchoux, H. Hantcherli, S. Mayer, H. Clemens and A. Couret,
615 Microstructures and mechanical properties of a multi-phase β-solidifying TiAl alloy densified
616 by spark plasma sintering, Acta Metall. Mater., 73 (2014) 107-115.

617 [27] Zghal S, Naka S, Couret A, A quantitative tem analysis of the lamellar microstructure in
618 TiAl based alloys, Acta Metall. Mater., 45 (1997) 3005-3015.

619 [28] M. Sabeena, A. George, S. Murugesan, R. Divakar, E. Mohandas, M. Vijayalakshmi,
620 Microstructural characterization of transformation products of bcc β in Ti-15 Mo alloy, Journal
621 of Alloys and Compounds, 658 (2016) 301-315.

622 [29] F. Delmas, M.J. Casanove, P. Lours, A. Couret, A. Coujou, Quantitative TEM study of the
623 precipitation microstructure in aluminium alloy Al(MgSiCu) 6056 T6. Material Science and
624 Engineering A 373 (2004) 80–89.

625 [30] J.S. Luo, T. Voisin, J.P. Monchoux, A. Couret A., Refinement of lamellar microstructures
626 by boron incorporation in GE-TiAl alloys processed by Spark Plasma Sintering, Intermetallics,
627 36 (2013) 12-20.

628 [31] G. Molénat, D. Caillard, Dislocation mechanisms in Ni,Al at room temperature. *In situ*
629 straining experiments in TEM, Phil. Mag. A, 64 (1991) 1291-1317.

630 [32] C. Bontemps, P. Veyssière, The geometrical configuration of kinks on screw
631 superdislocations in Ni,Al deformed at room temperature, Phil. Mag. Letters, 61 (1990) 259-
632 267.

633 [33] A. Couret, Y.Q. Sun, P.B. Hirsch, Glide sequences of deformation in the (111) plane of
634 Ni_3Ga single crystals in the yield stress anomaly, Phil. Mag. A, 67 (1993) 29-50.

635 [34] V. Paidar, M. Cak, Three types of dislocation core structure in B2 alloys, Intermetallics,
636 73 (2016) 21-25.

637 [35] P. Veyssière, R. Noebe, Weak-beam study of (111) superlattice dislocations in NiAl, Phil.
638 Mag. A, 65 (1992) 1-13.

639 [36] Y.Q. Sun, Characteristics of (111) slip in a NiAl [00l] single crystal, Phil. Mag. A, 80
640 (2000) 447-465.

641 [37] M. Legros, A. Couret, D. Caillard, Prismatic and basal slip in Ti_3Al : I. Frictional forces
642 on dislocations, Phil. Mag. A, 73 (1996) 61-80.

643 [38] A. Couret, D. Caillard, Dissociations and friction forces in metals and alloys. Journal de
644 Physique III, 1(6), (1991) 885–907.

645 [39] B. Viguier, K.J. Hemker, J. Bonneville, F. Louchet, J.L. Martin, Modeling the flow stress
646 anomaly in gamma TiAl. 1. Experimental observations of dislocation mechanisms, Phil. Mag.
647 A, 71 (1995) 1295-1312.

648 [40] S. Sriram, D.M. Dimiduk, P.M. Hazzledine, V.K. Vasudevan, The geometry and nature of
649 pinning points of 1/2 (110] unit dislocations in binary TiAl alloys, Phil. Mag. A, 76 (1997) 965-
650 993.

651 [41] A. Couret, An in situ study of ordinary dislocations glide in TiAl alloys, Phil. Mag. A, 79
652 (1999) 1977-1994.

653 [42] S. Zghal, A. Menand, A. Couret, Pinning points anchoring ordinary and Shockley
654 dislocations in TiAl alloys, Acta Mat., 46 (1998) 5899-5905.

655 [43] F. Delmas, M. Vivas, P. Lours, M.J. Casanove, A. Couret, A. Coujou, Straining
656 mechanisms in aluminium alloy 6056. In-situ investigation by transmission electron
657 microscopy. Material Science and Engineering A 340 (2003) 286–291.

[44] F. Pettinari, M. Prem, G. Krexner, P. Caron, A. Coujou, H.O. Kirchner, N. Clemént, Local order in industrial and model γ phases of superalloys. Acta Materialia, 49(13), (2001) 2549–2556.